Resonance Energy Transfer Mediated by Metal-Dielectric Composite Nanostructures

Noor Eldabagh,[†] Matthew Micek,[†] A. Eugene DePrince, III,[‡] and Jonathan J. Foley IV[*,†]

†*Department of Chemistry, William Paterson University, 300 Pompton Road, Wayne, NJ, 07470, USA*

‡*Department of Chemistry and Biochemistry, Florida State University, Tallahassee, Florida 32306-4390, United States*

E-mail: foleyj10@wpunj.edu

Abstract

Nanostructure-mediated energy transfer has attracted considerable attention as a template for photocatalysis and solar energy conversion, and the use of noble metal nanoparticles that support localized surface plasmon resonances (LSPRs) has been widely explored as a medium for realizing this paradigm. On the other hand, composite nanoparticles (CNPs) comprised of a large dielectric bead and smaller metal nanostructures have been shown to achieve efficient energy transfer to small-molecule adsorbates through the interplay between dielectric scattering resonances and the broad-band absorption associated with the metal nanostructure. This scattering mediated absorption can enable selective photochemistry without relying on the plasmonic properties of noble metal nanoparticles. While the precise photochemical mechanisms themselves remain unknown, resonance energy transfer (RET) is one feasible route for initiating the photochemistry. We demonstrate computationally that CNPs indeed facilitate RET to small-molecule adsorbates and that CNPs offer a framework in which one can design RET donors that outperform typical plasmonic nanoparticles employed within LSPR-driven RET under comparable illumination conditions. We also exploit the tunability of the resonances on the CNPs to realize strong coupling between the CNP and LSPR modes.

Introduction

Resonance energy transfer (RET) is a process that permits the directed flow of optical energy through systems comprised of multiple chromophores, the most familiar example of which being the transfer of energy in photosynthetic light harvesting complexes.[1–5] This non-radiative energy transfer mechanism occurs when the oscillating transition dipole moment of a donor species, initially excited by an external electromagnetic field, exerts a potential that induces a second oscillating transition dipole moment in a nearby acceptor species.[6]

The strength of this potential, and therefore the RET rate, depends on the magnitudes, relative orientation, and spatial proximity of the donor and acceptor transition dipole moments, as well as on the overlap in the frequency of the dipole oscillations. Generally speaking, large RET rates require large overlap between the donor and acceptor dipole moments and frequencies, and donor-acceptor separations of a few nanometers or less. The sensitivity of the RET rate to these parameters has led to the development of RET as a probe for the nanoscale structure of complex molecular and biomolecular systems.[7]

Substantial effort has recently been focused on the development of nanoscale systems with RET donor and acceptor components that are capable of highly-efficient and selective transfer of optical energy.[3,7–14] Common features of the donors and acceptors in such engineered systems include strong intrinsic optical resonances. The large transition dipole moments and tunable excitation energies associated with quantum dots (QD) and semiconductor nanoplatlets make them promising candidates as efficient RET donors and acceptors.[7,14,15] Similarly, engineered molecular systems, including J-aggregates[12,13] and QD-J-Aggregate hybrids[16–18] have been studied as platforms for nanoscale RET. Plasmonic resonances also tend to display large transition dipoles, so noble metal nanoparticles form another class of potential RET donors to molecules,[18–23] semi-conductors,[10,11] and to other plasmonic nanoparticles.[24–26] However, the competition between energy transfer and relaxation events becomes particularly important for determining the efficacy of RET in plasmonic systems.

Molecular self-assembly, for example using DNA as a ligand, has enabled the realization of nanoengineered composites for studying and controlling RET.[27–34] Indeed, it has been established that nanoparticles made of gold[35] can be attached to DNA by adding a thiol or disulfide moiety on either end (5' or 3') of the oligonucleotide, and adsorbing that surface to the nanoparticle,[36] and subsequent developments have permitted binding of DNA templates to silver.[27] The binding of DNA to other metals such as palladium and platinum has been less successful because there is greater competition by other oxidizing agents to displace the thiol-modified oligonucleotide, and because of the weaker affinity of thiol groups to the other metals compared to gold.

In this work, we computationally investigate RET initiated by emergent optical resonances, herein called *scattering mediated absorption* (SMA) resonances, in composite nanoparticles comprised of a large (100s of nm) dielectric nanosphere decorated on the surface with small-diameter ($<$ 10 nm) metal nanospheres. These composite nanoparticles (CNPs) are illustrated schematically in Figure 1. SMA has been discussed in several different experimentally-realized and theoretical platforms involving dielectric/metal[37–39] and dielectric/semiconductor CNPs.[40,41] The large dielectric bead of the CNPs can support a variety of optical scattering resonances (e.g. whispering gallery modes) that arise from the boundaries placed upon the light field by the geometry and dielectric contrast associated with the bead and its interface with the surrounding. Whispering gallery mode resonances in particular concentrate optical energy near the surface of the bead and have evanescent tails that penetrate into the surrounding medium. Metal nanoparticles at or near the surface of the bead can be excited by these evanescent fields which leads to strong absorption of the scattered light, hence the term scattering mediated absorption. A key feature of CNPs that support SMA is that their absorption spectra mimics the resonance position, intensity, and linewidths of the scattering spectra of the dielectric bead component. Because these SMA absorption peaks are associated with strong charge density oscillations on the metal sites themselves,[39] we propose that SMA resonances may show promise for efficient RET with a particularly promising feature being that the magnitude and frequency of their transition dipoles, as well as their resonance lifetimes, can be controlled via the geometry of the underlying dielectric nanostructure. Because SMA relies upon the scattering resonances in the dielectric component, not on the intrinsic resonant properties of the metal components, CNPs offer considerable versatility in designing RET donors that goes beyond that of purely plasmonic donors. Further, this flexibility creates opportunities to select metal components based on other important considerations like favorable chemistry with RET acceptors, stability, earth abundance, biocompatibility, etc.

We develop a simple quantum dynamical model of RET driven by SMA in CNPs. We consider RET to small molecule acceptors, where the molecular component is parameterized as malachite green (MG), and we show
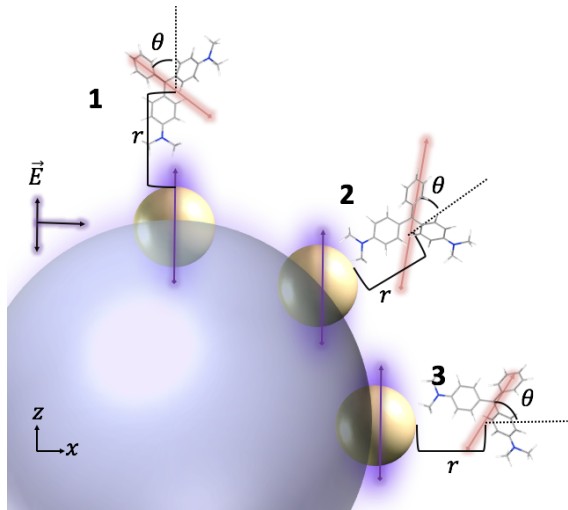
Figure 1: Illustration of several possible orientations of MG molecules on a given CNP. From Ref. 22, we assume $r = 2.54$ nm and $\theta = 60°$. As seen in orientation 2, there will likely be some adsorbed molecules where the orientation of the acceptors transition dipole moment with close alignment of the transition dipole moments of the donor and acceptor. In the main text, we consider the scenario illustrated as Configuration **2** where the displacement vector between the NP and the molecule is $-45°$ with respect to the polarization direction of the incident field (the z-axis), leading to a relative angle of $-15°$ between the donor and acceptor transition dipole moments.

that efficient RET to MG is indeed possible using CNP donors. We also consider simple assemblies of the CNPs tethered to plasmonic nanoparticles, which could be experimentally realized using DNA templating, and we show that strong coupling between the CNPs and the plasmonic nanoparticles may be realized under experimentally feasible geometries. Our results suggest that these CNPs show exceptional promise as RET donors and as building blocks for assemblies that can realize strong coupling between light and matter.

Theory

Resonance energy transfer in nanoscale and hybrid nanoscale/molecular systems represents a challenging multi-scale problem for theory and simulation, and a rich body of literature describes strategies to bridge the relevant nanoscale/molecular and photonic/electronic degrees of freedom. Recently, Lopata and co-workers[22] employed a mixed classical/quantum-mechanical approach that propagates classical equations of motion for the electric field in a nanoscale environment and quantum-mechanical equations of motion for the electronic degrees of freedom in a molecular system. Fully quantum-mechanical models for excitation energy transport in nanoscale systems have also been proposed, wherein, for example, plasmonic system components can be treated using time-dependent density functional tight binding[26] or within the framework of cavity quantum electrodynamics (CQED).[21] While some studies employ *ab initio* electronic structure descriptions of molecular system components (using, for example, Hartree-Fock[21] or density functional theory[42]), many adopt simpler schemes in which complex molecular systems are modeled via effective Hamiltonians.[2,15,22,43–45] In these cases, model Hamiltonian parameters can be obtained from theoretical computations[46] or experiment.[47] We adopt this simpler approach and solve quantum-mechanical equations of motion for coupled donor/acceptor systems, each described by a simple model Hamiltonian.

The dynamics of a CNP donor (D) coupled to a molecular or nanoparticle acceptor (A) are governed by coupled Liouville-Lindblad equations of motion,

$$\frac{d}{dt}\rho_D = -i[H_D, \rho_D] + L_D(\rho_D), \qquad (1)$$

$$\frac{d}{dt}\rho_A = -i[H_A, \rho_A] + L_A(\rho_A), \qquad (2)$$

where ρ_D (ρ_A) and H_D (H_A) denote the density and Hamiltonian matrices for the donor (acceptor), respectively, and L_D (L_A) represents the Lindblad operator for the donor (acceptor). Here, the equations of motion are expressed using atomic units. The Hamiltonian operators for the donor and acceptor are defined as

$$\hat{H}_D = \hat{H}_{0,D} - \hat{\mu}_D \cdot \mathbf{E}(t) + \hat{V}^{A \to D}, \qquad (3)$$

and

$$\hat{H}_A = \hat{H}_{0,A} - \hat{\mu}_A \cdot \mathbf{E}(t) + \hat{V}^{D \to A}, \qquad (4)$$

where $\hat{H}_{0,X}$ denotes the field-free contribution of the uncoupled donor ($X = D$) or acceptor ($X = A$) system, $\hat{\mu}_X$ represents the dipole operator for the donor or acceptor, $\mathbf{E}(t)$ denotes the external electromagnetic field, and $\hat{V}^{D \to A}$ and $\hat{V}^{A \to D}$ describe the influece of the donor dipole moment on the acceptor and *vice versa*. All matrix elements are expressed in the basis of energy eigenstates of the uncoupled donor or acceptor, in which the matrix representations of $\hat{H}_{0,A}$ and $\hat{H}_{0,D}$ are diagonal.

Implicit in Eqs. (3) and (4) is the assumption that the donor and acceptor interact only through their transition dipole moments. The associated dipole potential operators are two-body operators, in which case correct equations of motion for the one-body density matrices, ρ_D and ρ_A, should depend on a two-body donor-acceptor density matrix. We eliminate the dependence of the equations of motion on the two-body density matrix by further assuming that the transition dipoles of the acceptor interacts only with the instantaneous expectation value of the dipole moment of the donor and *vice versa*. The interaction potential operator for the donor, in atomic units, is then given by

$$\hat{V}^{A \to D} = \frac{1}{n^2 r^3}\left(\hat{\mu}_D \cdot \langle\mu_A\rangle - 3\frac{(\hat{\mu}_D \cdot \mathbf{r})(\mathbf{r} \cdot \langle\mu_A\rangle)}{r^2}\right), \qquad (5)$$

where n is the refractive index of the surrounding medium (taken to be water, with $n = 1.33$, throughout); an analogous expression defines the interaction potential operator for the acceptor. This treatment is similar to that employed in the hybrid CQED/*ab initio* electronic structure model of plasmon-molecule interactions described in Ref. 21. The potential defined in Equation (5) is a point dipole approximation to the interaction between the donor and the acceptor, which may break down when the length-scale of separation between the donor and acceptor is similar to the length-scale of the donor/acceptor itself, or when there are higher multipolar contributions to the charge density oscillations that drive the interaction;[3,48] both limitations to the point-dipole approximation may be important in the systems studied herein. An approach to the interaction potential that overcomes these limitations is provided by the transition density cube method, which provides the full Coulombic interaction between the charge density oscillations on donor and acceptor species to within the accuracy of the level of theory used to compute the many-electron wavefunction of the donor and acceptor.[49] However, calculation of the requisite many-electron wavefunction for nanoparticles, even at low levels of theory, represents a considerable computational challenge and is beyond the scope of this work.

The absorption and scattering spectra of the donor and acceptor are computed using the Fourier transform of the dipole expectation values and the incident field. The absorption cross section is given by

$$\sigma_{abs}(\omega) = \frac{k}{\epsilon_0}\text{Im}(\alpha(\omega)), \qquad (6)$$

and the scattering cross section is given by

$$\sigma_{scat}(\omega) = \frac{k^4}{6\pi\epsilon_0^2}|\alpha(\omega)|^2, \qquad (7)$$

where $k = n\frac{\omega}{c}$ is the wavenumber at the angular frequency ω. The polarizability, $\alpha(\omega)$, is determined by

$$\alpha(\omega) = \frac{\int_0^T e^{i\omega t}\mu(t)dt}{n^2 \int_0^T e^{i\omega t}E(t)dt}. \tag{8}$$

where T represents the total simulation time. We use the enhancement in scattering of the acceptor when coupled to the donor over that of isolated acceptor as a measure of RET. As discussed below, we also monitor energy transfer to molecular acceptors through the population of a sink state that can only be accessed through excited-state relaxation on the acceptor.

Modeling Nanoparticle Donors

The CNP donors are modeled as quantum systems with N_D levels and $N_D - 1$ optically-allowed transitions, where N_D is a system-dependent parameter (usually ≈ 10). As an illustrative example, consider the five-level system depicted in Figure 2 (N_D=5). In this case, the field-free Hamiltonian matrix is

$$\mathbf{H}_0 = \begin{pmatrix} 0 & 0 & 0 & 0 & 0 \\ 0 & \epsilon_2 & 0 & 0 & 0 \\ 0 & 0 & \epsilon_3 & 0 & 0 \\ 0 & 0 & 0 & \epsilon_4 & 0 \\ 0 & 0 & 0 & 0 & \epsilon_5 \end{pmatrix}, \tag{9}$$

where ϵ_i represents the energy of the ith state, relative to that of the ground state, and the dipole matrix has the form

$$\mu = \begin{pmatrix} 0 & \mu_{12} & \mu_{13} & \mu_{14} & \mu_{15} \\ \mu_{21} & 0 & 0 & 0 & 0 \\ \mu_{31} & 0 & 0 & 0 & 0 \\ \mu_{41} & 0 & 0 & 0 & 0 \\ \mu_{51} & 0 & 0 & 0 & 0 \end{pmatrix}. \tag{10}$$

The optically-allowed transitions are between the ground state and any excited state, i, and the corresponding transition dipole matrix elements are denoted μ_{1i}/μ_{i1}. The parameters ϵ_i and μ_{1i}/μ_{i1}, as well as lifetime parameters that enter into the Lindblad operator, are extracted from finite-difference time-domain (FDTD) simulations of the optical re-
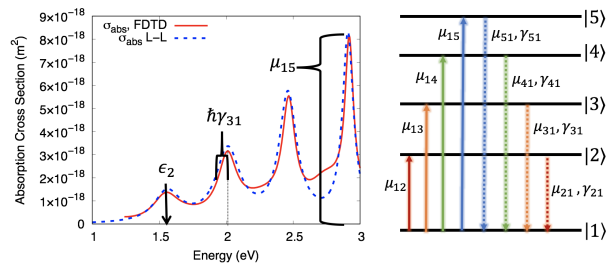

Figure 2: Jablonski diagram of a hypothetical CNP with 4 optically-allowed transitions between state $|1\rangle$ and states $|2\rangle$, $|3\rangle$, $|4\rangle$, and $|5\rangle$. Each excited state can undergo spontaneous emission with a rate associated with γ.

sponse of the CNPs. Observed absorption features in the FDTD simulations map directly onto the excitation energies, ϵ_i, and the area under each absorption peak can be used to determine the transition dipole moments.[18] Lastly, the half-width at half-maximum of each absorption peak yields relaxation rates, γ_{i1}, which enter into the Lindablad operator

$$L_D = \sum_{i\neq 1}^{N_D} 2\gamma_{i1}\langle i|\rho_D|i\rangle|1\rangle\langle 1| - \gamma_{i1}\{|i\rangle\langle i|, \rho_D\}. \tag{11}$$

Figure 2 illustrates the relationship between these parameters and an FDTD-derived absorption spectrum. Also provided is the spectrum generated according to the solution of the equation of motion for the donor, in the absence of the acceptor, using the parameterized model Hamiltonian. The model Hamiltonian yields a spectrum that is in reasonable agreement with that from the electrodynamics simulations, and we note that the absorption features can be attributed to the metal components of the CNP, as the dielectric is lossless in this energy window. Details of the electrodynamics simulations and the treatment of the CNPs within these simulations can be found in the Supporting Information (SI).

We are interested in the RET donor properties of CNPs comprised of a dielectric nanosphere decorated with small (5 nm diameter) platinum nanospheres. We consider two CNPs with dielectric components having

5

diameters of 400 nm (denoted CNP400) or 600 nm (denoted CNP600). In both cases, the refractive index of the dielectric bead is taken to be $n = 2.6$, and the CNP is immersed in a surrounding medium with a refractive index of $n = 1.33$. We focus on the limit of small coverage of the metal nanoparticles, where a typical energy transfer event will likely occur between a discrete metal nanoparticle component of the CNP and one or more acceptor molecules that are adsorbed to its surface. Specifically, each CNP is decorated with only eight platinum nanospheres, which are equally spaced along the great circle of the sphere that contains the propagation plane of the incident light.

We also compare RET donor performance of the CNPs to lone plasmonic nanoparticles, which are modeled as 5 nm spherical silver and gold nanoparticles embedded in the same surrounding medium ($n = 1.33$). Hamiltonian and Lindbladian parameters for the plasmonic donors were obtained in a manner similar to that described above, except that analytical absorption spectra were obtained from Mie theory rather than FDTD simulations. We use the permittivity data of Palik[50] for platinum in our electrodynamics simulations, and permittivity data of Johnson and Christy is used for gold and silver.[51] Due to the small size of the plasmonic nanoparticles and the metal components of the CNPs, quantum size effects are expected to play a role in the spectral response.[52–56] We account for these size effects by introducing a phenomenological correction to the intraband contribution to the permittivity; we do not consider size corrections to the interband contribution to the permittivity which have been theoretically shown to converge to the bulk limit for sizes smaller than the nanoparticles considered in this work[57,58]. The details for the intraband correction, as well as tables of Hamiltonian and Lindbladian parameters, can be found in the SI (see Tables S1, S2, and S3).

Modeling Acceptor Systems

In this work, we consider both small-molecule dyes and plasmonic nanoparticles as acceptors, and the relevant Hamiltonian and Lind-

bladian parameters can be extracted from experimentally obtained or simulated absorption spectra. The metal nanoparticle acceptors are modeled as 5 nm silver or gold particles, as described above, and the small-molecule dyes are modeled after malachite green (MG). We
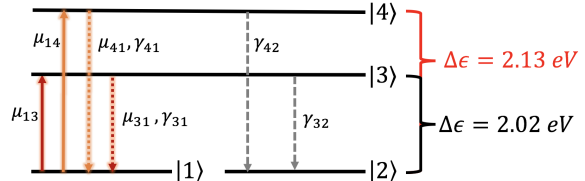
Figure 3: Jablonski diagram corresponding to the 4-level model of malachite green with 2 optically allowed transitions between state $|1\rangle$ and states $|3\rangle$ and $|4\rangle$. States $|3\rangle$ and $|4\rangle$ can undergo non-radiative relaxation to state $|2\rangle$ with rates γ_{32} and γ_{42}, respectively. Radiative relaxation of these excited states to state $|1\rangle$ with rates γ_{31} and γ_{41} could also be modeled, but due to the small fluorescence quantum yield of malachite green, we neglect these channels in this work. State $|2\rangle$, termed the "sink state", is degenerate with $|1\rangle$ and has no optically-allowed transitions to other states; hence, population transferred to $|2\rangle$ cannot be redistributed to other states.

take the Hamiltonian and Lindbladian parameters for MG from the work of Lopata and coworkers,[22] who examined the coupled optical response of gold nanoparticles and MG. In that study, the optical response of the dye, which was described as a three-level quantum system, was embedded within a classical electrodynamics simulation for the nanoparticle. Here, we slightly modify the quantum model for MG to include four levels: the ground state ($|1\rangle$), a sink state ($|2\rangle$) that is degenerate with the ground state, and two excited states ($|3\rangle$ and $|4\rangle$) with optically-allowed transitions from/to state $|1\rangle$; these transitions give rise to absorption features depicted in Figure 3. Because there are no optically-allowed transitions to the sink state ($|2\rangle$), relaxation from states $|3\rangle$ and $|4\rangle$ to the this state is purely non-radiative and

is modeled by the Lindbladian terms

$$L_{\text{nonrad}} = \sum_{i=3}^{4} 2\gamma_{i2}\langle i|\rho_A|i\rangle|2\rangle\langle 2| - \gamma_{i2}\{|i\rangle\langle i|, \rho_A\}.$$

$$(12)$$

Further, since there are no optically-allowed transitions to or from $|2\rangle$, population in this state reflects the cumulative population transferred to the excited states of MG through coupling to either the external field or to the dipole field of the CNP. Hence, the relative sink population in the isolated acceptor and coupled donor-acceptor systems can be used as a measure of RET efficiency. This differs from a common experimental measure of RET efficiency to acceptor fluorophores, which uses fluorescence enhancement of the acceptor to define a RET quantum yield per excitation event of the donor;[59] while we could adopt this measure in our simulations, we find the definition in terms of sink populations to be simpler in this case. Radiative relaxation channels, namely fluorescence, in MG may also included in the present model through the Lindbladian terms

$$L_{\text{rad}} = \sum_{i=3}^{4} 2\gamma_{i1}\langle i|\rho_A|i\rangle|1\rangle\langle 1| - \gamma_{i1}\{|i\rangle\langle i|, \rho_A\},$$

$$(13)$$

and the total Lindblad operator for the acceptor is

$$L_A = L_{\text{rad}} + L_{\text{nonrad}}. \qquad (14)$$

Because the fluorescence quantum yield of MG is extremely low,[60] we neglect L_{rad} in all calculations herein, meaning all dissipation on MG is radiationless. The Hamiltonian and Lindbladian parameters for MG are given in Table 1.

In all computations, we assume a single MG molecule is adsorbed to the surface of a single metal nanoparticle. This situation differs from that considered by Lopata and co-workers,[22] in which a 80 nm gold nanoparticle was coated with a monolayer of 9200 MG molecules. Nonetheless, the present assumption is not too dissimilar from the case in Ref. 22.

Table 1: Hamiltonian and Lindbladian parameters for malachite green quantum model taken from Ref. 22. Note that $N = 1$ denotes the ground energy eigenstate and all energies are relative to the ground state energy, hence $\epsilon_1 = 0$. Similarly, it is assumed that only transitions between the ground state and the excited-states contribute to the spectra, transitions between the excited-states are not considered in this model.

State N	1	2	3	4
ϵ_N (eV)	0	0	2.02	2.13
μ_{1N} (D)	0	0	5.046	4.003
γ_{N1} (THz)	0	0	0	0
γ_{N2} (THz)	0	0	85.8	141.6

The metallic components of the CNPs are much smaller (5 nm), and, with the same density of adsorbates, a full monolayer of MG would consist of only ≈ 35 molecules. We also note that in the CNPs, each metal may be partially embedded in the dielectric nanosphere, further reducing the available surface area for adsorption.

Following Ref. 22, we assume that the separation between the center of mass of the molecule and the nanoparticle is 2.5 nm and that the transition dipole of MG is aligned at a 60° angle, relative to the nanoparticle surface normal. This geometry introduces the possibility of a variety of angles of the MG transition dipole relative to the transition dipole of the CNP donor depending on where the metal NP is located with respect to the polarization axis of the CNP; Figure 1 depicts three such possibilities. We consider the specific scenario that gives rise to a relative angle of the transition dipole of the donor and acceptor of −15° (configuration **2** in Figure 1).

We have considered several limiting cases to validate the present quantum model. In particular, we confirmed that the Hamiltonian and Lindbladian contributions parameterized as described yield absorption spectra in agreement with those obtained from rigorous electrodynamics simulations. Further, we have confirmed that the RET efficiency as a function of donor-acceptor separation simulated by our method exhibits the expected $1/r^6$ dependence

(see Figures S1 and S2 in the SI). We also perform FDTD calculations of the electric field at the surface of an acceptor nanoparticle at various separations from a donor HNP as a classical electrodynamics analog of the RET phenomenon we are studying. We find that the magnitude of the induced electric field on the acceptor as a function of separation can be reasonably approximated by a $1/r^6$ function, which suggests a strong dipolar contribution to the near-field interactions. Deviations from perfect $1/r^6$ behavior could result from higher-order multipolar contributions to the nearfields of the metal nanoparticles, and also from the evanescent fields from the dielectric scattering resonances (see Figure S3)

Results and Discussion

We first consider the case in which the RET acceptor, MG, is adsorbed to a CNP RET donor (either CNP400 or CNP600). Specifically, MG is modeled as being adsorbed to the small metal nanoparticle constituent of the CNP. Unless otherwise indicated, we excite the system with a short (3.62 fs) pulse centered at 2.02 eV with a peak field strength of $5.14 \cdot 10^7$ V/m. The center frequency of this pulse was chosen to overlap with the absorption resonances in MG, and the short pulse duration leads to a broad energy distribution spanning the visible and near-UV range, which is the energy range over which the nanostructures studied here have strong resonant properties.

The absorption spectra of the CNPs (which can be found in Figure S1 in the SI) indicate that the optical response of the CNPs can be dramatically tuned by changing the diameter of the underlying dielectric bead. Not only can the energies of the resonances be tuned this way, but their oscillator strength and lifetimes also depend on the diameter. The two CNPs studied here were chosen because they have SMA resonances at around 2 eV, giving good overlap between at least one SMA resonance and the absorption resonances in MG, which occur at at 2.02 and 2.13 eV. For example, CNP600 has a series of SMA resonances with strong oscillator strengths at energies of 1.98 eV, 2.20 eV, and 2.27 eV. CNP400 has a strong SMA resonance at 2.04 eV with almost perfect overlap with the lower energy absorption resonance in MG; however, the oscillator strength for this resonance is slightly smaller than those in CNP600.

Figures 4 and 5 provide strong evidence of RET in the coupled MG-CNP systems. First, we observe dramatic enhancement in the scattering of MG, with the greatest enhancement arising in the case of CNP400, despite the fact that the SMA resonances in CNP600 have larger oscillator strengths and can thus exert a stronger potential upon the acceptor through its transition dipole moment. The superior scattering enhancement from CNP400 can be attributed in part to greater overlap between the absorption features in MG with the SMA resonances in CNP400, as compared to the overlap with those in CNP600. Further, the dipole trajectory of CNP600 shows evidence of interferences between the transition dipoles associated with the multiple SMA resonances. The coupled CNP600-MG system displays a larger induced dipole moment than the uncoupled MG system displays at early times following the excitation of the system. However, the induced dipole in the coupled system decays rapidly (see Figure 4). This behavior contrasts with that of the CNP400-MG system, where the dipole moment of the coupled systems persists for longer than that of uncoupled MG. As a consequence, the CNP600-MG system shows a noticeable broadening in its scattering spectrum, while the CNP400-MG system actually shows a narrowing in the scattering spectrum. Both systems show considerable enhancement in population transferred to the sink state of MG, which is another important measure of the RET efficiency. Both coupled systems show nearly a 100-fold increase in population transfer as compared to the lone MG system under the same excitation conditions; the uncoupled system has a final sink population of 7.75×10^{-5}, as compared to populations of 4.8×10^{-3} and 6.8×10^{-3} for the CNP400-MG and CNP600-MG systems, respectively. The sink populations encapsulate both the light-harvesting and RET efficiency of the nanoparticle systems; that is, the CNP600-

MG system in this case is seen to have a larger final sink population, but the larger absorption cross section of the CNP600 system also implies that it will absorb more of the incident optical energy under the same illumination conditions.

In order to better quantify the RET efficiency irrespective of light harvesting potential, we also report the final population of the sink state on MG relative to the maximum hole population of state $|1\rangle$ on the donor systems, which we denote $Q_D(1,1) = 1 - \rho_D(1,1)$. The final sink population on MG divided by the maximum hole population on the donor is a rough estimate of the RET efficiency that is normalized for light-harvesting potential of the donor species. The quantity $\eta = \rho_A^{final}(2,2)/Q_D^{max}(1,1)$ is tabulated in Table 2. This analysis indicates that the CNP400-MG system displays both greater scattering enhancement and greater RET efficiency relative to the fraction of incident energy absorbed by the donor, while the CNP600-MG shows greater absolute population transfer, which we attribute to the greater extinction of the CNP600 system along with the ability of the stronger coupling potential to drive more population to the excited states of MG in early times after the excitation (see Figures 4 and 5).

Table 2: Analysis of RET efficiency for the CNP and plasmonic nanoparticle systems. We report the maximum hole population on each donor, the final sink population on the acceptor, and the quotient of the two $\eta = \rho_A^{final}(2,2)/Q_D^{max}(1,1)$ as a measure of the RET transfer efficiency.

System	$Q_D^{max}(1,1)$	$\rho_A^{final}(2,2)$	η
CNP600	8.9×10^{-1}	6.8×10^{-3}	7.6×10^{-3}
CNP400	3.7×10^{-1}	4.8×10^{-3}	1.2×10^{-2}
Au	2.4×10^{-2}	2.0×10^{-4}	8.0×10^{-3}
Ag	3.3×10^{-2}	2.2×10^{-4}	6.6×10^{-3}

For comparison, indicators of RET efficiency are also computed for MG adsorbed to other RET donors, including lone silver, gold, and platinum nanoparticles (see Supporting Information, Figures S4, S5, and S6). Like the CNPs, the gold nanoparticle has a resonance
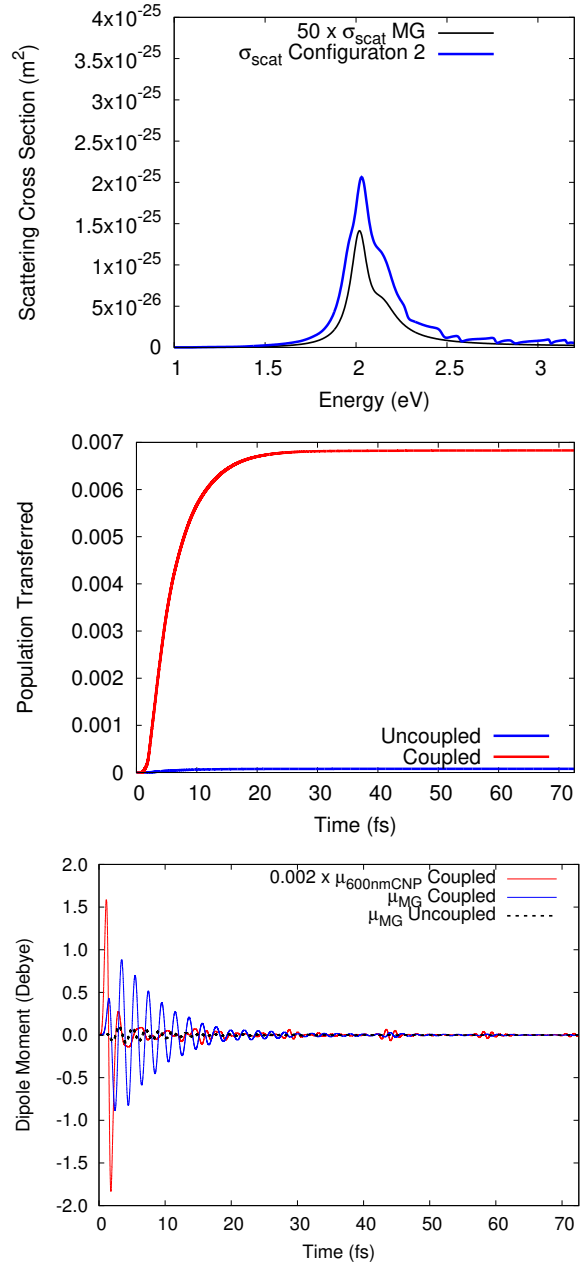

Figure 4: **Top** Scattering spectrum of MG coupled to CNP600 compared to lone scattering spectrum of MG. **Middle** Population transferred to the sink state of MG for MG coupled to CNP600 compared to population transferred to the sink state for lone MG (excited by the same incident pulse). **Bottom** Dipole expectation value as a function of time of CNP600 coupled to MG, MG coupled to CNP600, and lone MG excited by the same incident pulse.
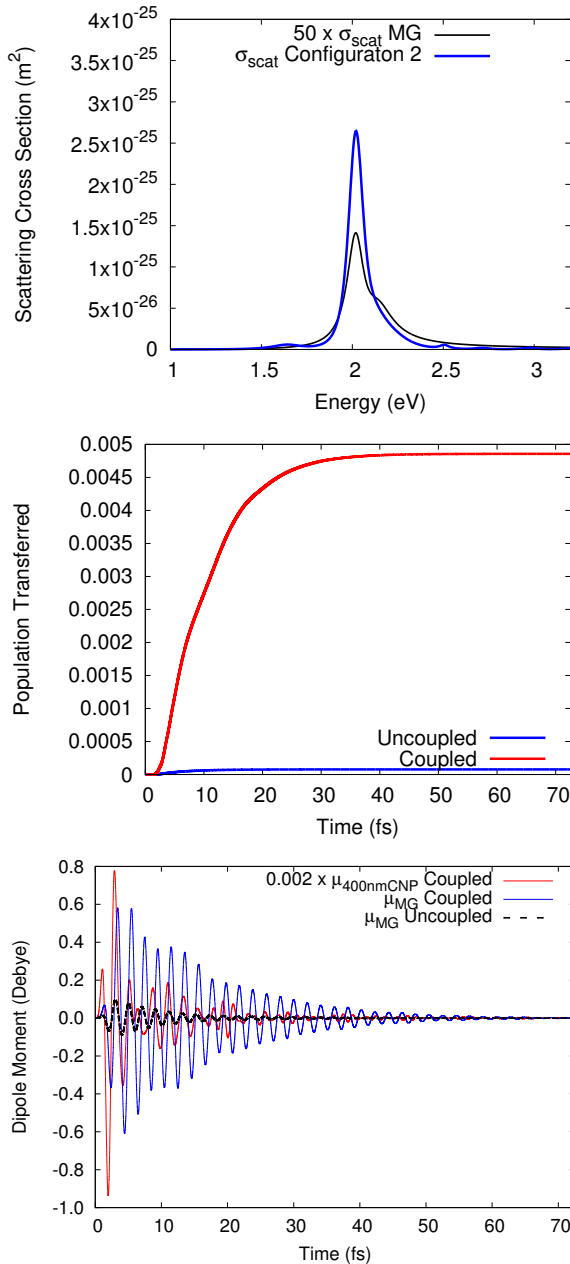
Figure 5: **Top** Scattering spectrum of MG coupled to CNP400 compared to lone scattering spectrum of MG. **Middle** Population transferred to the sink state of MG for MG coupled to CNP400 compared to population transferred to the sink state for lone MG (excited by the same incident pulse). **Bottom** Dipole expectation value as a function of time of CNP400 coupled to MG, MG coupled to CNP400, and lone MG excited by the same incident pulse.

with relatively strong spectral overlap with the absorption resonances of MG. On the other hand, the silver nanoparticle has a resonance that is 1 eV blueshifted (at 3.1 eV) and the platinum nanoparticle has a broad spectral feature that peaks at 4.5 eV. As can be seen in Table 2, the RET transfer efficiency, η, is smaller for silver and gold donors than for the CNP400 system. Coupling to lone metal nanoparticle donors, including gold (Figure S4) or silver (Figure S5) leads to enhancement in scattering and population transfer, but the effects are considerably weaker as compared to these effects when MG is coupled to the CNPs. Coupling to the lone plasmonic systems leads to roughly a 10-fold increase in population transfer: a final sink state population of 2.0×10^{-4} and 2.2×10^{-4} is observed for the Au-MG and Ag-MG systems, respectively. (see Figures S4, S5, and Table 2). We also consider RET to MG from a 5 nm platinum particle, which exhibits a very broad spectral feature in the UV range (see Figure S5 in the SI). Again we observe substantially lower RET efficiency in this system when compared to the CNPs decorated with the platinum nanospheres of the same size. We note that, because of the broadness of the absorption feature in the platinum nanoparticle, a shorter pulse (1.81 fs) was used for the lone platinum simulations. Because the illumination conditions were different for the lone platinum system, direct comparisons of the RET efficiency to other systems are not possible.

Strong Coupling to Plasmonic Nanoparticles

We now consider the situation where CNP donors are coupled to plasmonic metal nanoparticle acceptors, as illustrated in Figure 6; such assemblies may be realized using technology like DNA templating.[28–32] Our aim here is to explore the possibility of CNPs and plasmonic nanoparticles to form assemblies that can facilitate strong coupling between their resonances. In this context, strong coupling occurs when the interaction potential (V_{int}) between the two resonances is large compared decay rates of the resonances. Analysis of coupled two-level sys-
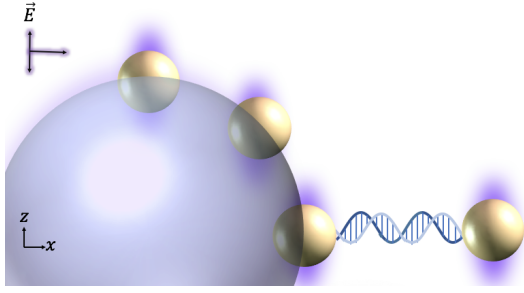
Figure 6: Illustration of a coupled CNP/Gold NP system using DNA templating, which can facilitate strongly coupled hybrid systems.

tems leads to the following rule of thumb: coupling is strong when $4V_{\text{int}} > \hbar(\gamma_1 + \gamma_2)$,[18,61] where γ_1 and γ_1 represent the relaxation rates for the two system components. The coupling potential is defined as

$$V_{\text{int}} = \frac{1}{n^2 r^3} \left(\boldsymbol{\mu}_{\text{SMA}} \cdot \boldsymbol{\mu}_P - 3 \frac{(\boldsymbol{\mu}_{\text{SMA}} \cdot \mathbf{R})(\mathbf{R} \cdot \boldsymbol{\mu}_P)}{r^2} \right),$$
(15)

where $\boldsymbol{\mu}_{\text{SMA}}$ and $\boldsymbol{\mu}_P$ is the transition dipole for a SMA or LSPR resonance on the CNP or plasmonic nanoparticle, respectively, and $\mathbf{R}$ is the separation vector between the particles. Clearly, multiple SMA resonances exist for each CNP, so we choose the resonance such that there is strong spectral overlap between the SMA resonance in the CNP and the plasmon resonance in the metal nanoparticle. In particular, we use Eq. 15 to compute the coupling strength between state $|8\rangle$ on CNP600 and the LSPR on gold, and the coupling strength between state $|13\rangle$ on CNP600 and the LSPR on silver. Choice of the resonance fixes the values of $\boldsymbol{\mu}$ and γ, so the conditions for strong coupling can be evaluated once the relative geometry (and hence $\mathbf{R}$) is specified. We compute the ratio $\frac{4V_{\text{int}}}{\gamma_{\text{SMA}}+\gamma_P}$ for a range of geometries where the plasmonic nanoparticles are displaced from the CNP by different separations and angles and plot these maps in Figures 7 and 8 in the main text and Figures S7 and S8 in the SI. Evaluating the maps of Eq. 15 for CNP600-Au and CNP600-Ag, the conditions for strong coupling ($\frac{4V_{\text{int}}}{\gamma_{\text{SMA}}+\gamma_P} > 1$) is predicted for both pairs at a variety of separations and configurations.

Similar maps and subsequent dynamics are also computed for CNP400-Au and CNP400-Ag in the SI (see Figures S7 and S8, respectively).

Strong coupling between two optically-excited systems leads to distinct features in their coupled dynamics that can dramatically alter observable, including their absorption and scattering cross sections. In particular, strong coupling permits the exchange of excitation energy between the systems on timescales that are faster than dissipative timescales. We see evidence of these dynamics in both the CNP600-Au and CNP600-Au systems through their dipole trajectories, which show much slower decay than compared to the lone plasmonic nanoparticles (see Figure 7 and 8). We also see a periodic recurrence, or beating, of amplitude of the coupled dipole moments, that is characteristic of the strong coupling limit. We also observe significant changes in the scattering spectrum, including splitting of the plasmon resonances (see Figures 7 and 8), which are another indicator of the strong coupling limit.

Conclusion

We have developed a simple quantum dynamical model of resonance energy transfer driven by emergent resonances, known as scattering mediated absorption resonances, in composite nanoparticles. Importantly, we have shown that such composite nanoparticles can be used as versatile RET donors, owing to the fact that the energy, intensity, and lifetime of the SMA resonances may be controlled by simple geometric parameters of the composites. Applying our quantum dynamical model demonstrated superior RET efficiency may be possible using these composites as compared to plasmonic nanoparticles of similar size. We also proposed assemblies of composite nanoparticles and plasmonic nanoparticles that leverages well-developed DNA-based nanotechnology for creating super-assemblies of nanoparticles with well-controlled spacing and orientation, and showed that such assemblies may be used to realize strong coupling between the CNPs and plasmonic particles. Our results sug-
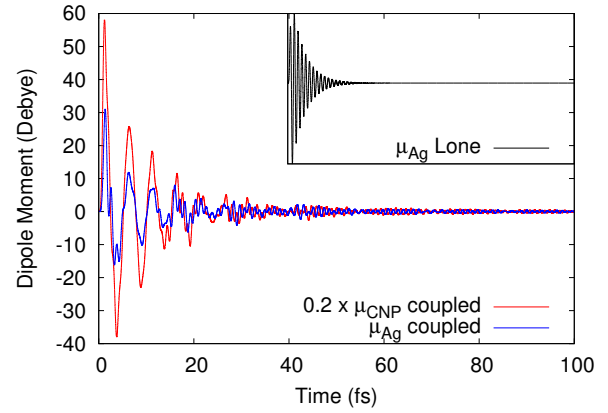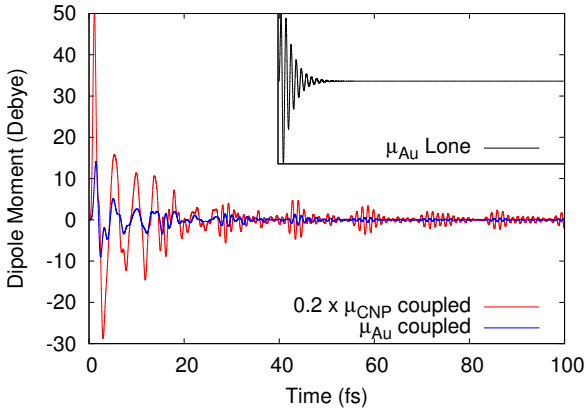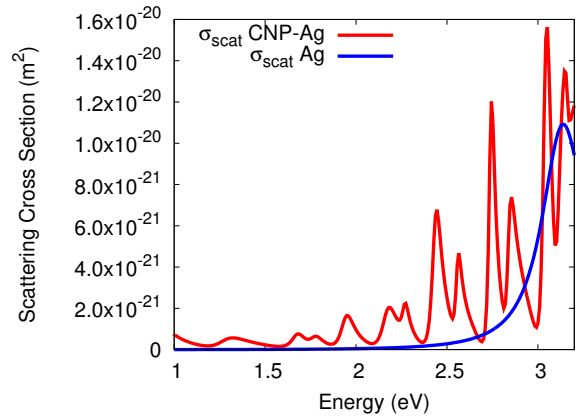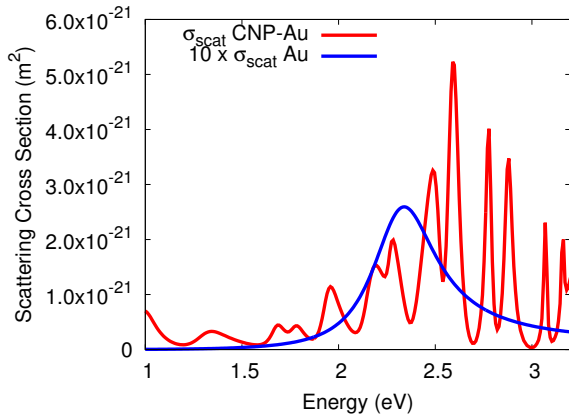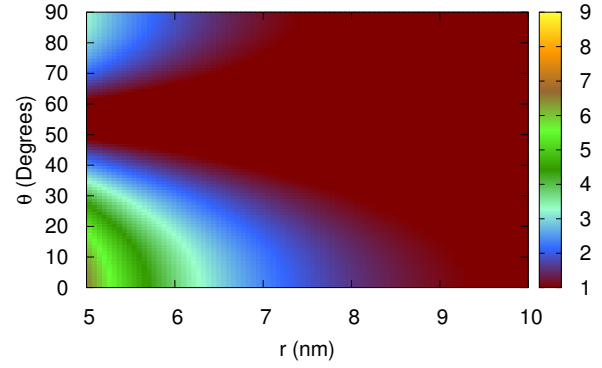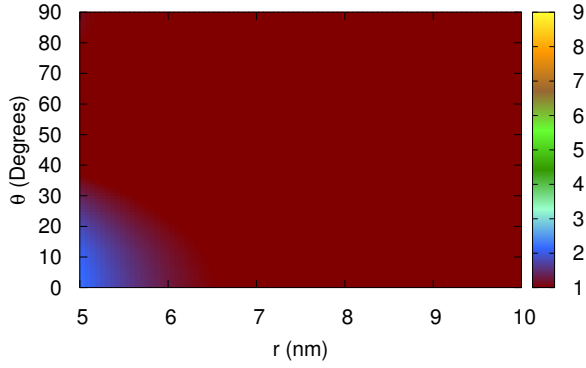
11

Figure 7: 600 nm CNP - 5 nm Au nanoparticle separated by $r = 7$ nm. **Top**: Ratio of coupling strength to dissipation rate $(4V_{\text{int}}/(\gamma_{\text{SMA}} + \gamma_P))$ for matched resonances in the CNP/Au stem. **Middle**: Scattering spectrum of lone-Au compared to CNP-Au coupled system. **Bottom**: Dipole moment trajectory for CNP and Au in the coupled system compared to lone Au system (inset).

Figure 8: 600 nm CNP - 5 nm Ag nanoparticle separated by $r = 7$ nm. **Top**: Ratio of coupling strength to dissipation rate $(4V_{\text{int}}/(\gamma_{\text{SMA}} + \gamma_P))$ for matched resonances in the CNP/Ag stem. **Middle**: Scattering spectrum of lone-Ag compared to CNP-Ag coupled system. **Bottom**: Dipole moment trajectory for CNP and Ag in the coupled system compared to lone Ag system (inset).

gest that these composite nanostructures, and assemblies involving them, may have important implications for light harvesting, energy transfer, and the control of chemical reactions through the paradigm of polaritonic chemistry.

Associated Content

Supporting Information. Supporting details on the finite-different time-domain simulations, supporting data tables, and supporting figures are provided in the Supporting Information. This material is available free of charge via the Internet at http://pubs.acs.org

Author Information

Corresponding Author

* Email: foleyj10@wpunj.edu

The authors declare no competing financial interest.

Acknowledgment

References

(1) Blankenship, R. E. *Molecular Mechanisms of Photosynthesis*; Blackwell Science, 2002.

(2) Wu, J.; Liu, F.; Shen, Y.; Cao, J.; Silbey, R. J. Efficient energy transfer in light-harvesting systems, I: optimal temperature, reorganization energy and spatial-temporal correlations. *New. J. Phys.* **2010**, *12*, 105012.

(3) Scholes, G. D. Long-range resonance energy transfer in molecular systems. *Annu. Rev. Phys. Chem.* **2003**, *54*, 57–87.

(4) Hayes, D.; Panitchayangkoon, G.; Fransted, K. A.; Caram, J. R.; Wen, J.; Freed, K. F.; Engel, G. S. Dynamics of electronic dephasing in the Fenna-Matthews-Olson complex. *New J. Phys.* **2011**, *12*, 065042.

(5) Hayes, D.; Wen, J.; Panitchayangkoon, G.; Blankenship, R. E.; Engel, G. S. Robustness of electronic coherence in the Fenna-Matthews-Olson complex to vibronic and structural modifications. *Faraday Discuss.* **2011**, *150*, 459–469.

(6) Andrews, D. L.; Curutchet, C.; Scholes, G. D. Resonance energy transfer: Beyond the limits. *Laser Photonics Rev.* **2011**, *5*, 114–123.

(7) Hildebrandt, N.; Spillmann, C. M.; Algar, W. R.; Pons, T.; Stewart, M. H.; Oh, E.; Susumu, K.; Daz, S. A.; Delehanty, J. B.; Medintz, I. L. Energy Transfer with Semiconductor Quantum Dot Bioconjugates: A Versatile Platform for Biosensing, Energy Harvesting, and Other Developing Applications. *Chemical Reviews* **2017**, *117*, 536–711.

(8) Choi, Y.; Kang, T.; Lee, L. P. Plasmon Resonance Energy Transfer (PRET)-based Molecular Imaging of Cytochrome c in Living Cells. *Nano Letters* **2009**, *9*, 85–90.

(9) Han, Y.; Noor, M. O.; Sedighi, A.; Uddayasankar, U.; Doughan, S.; Krull, U. J. Inorganic Nanoparticles as Donors in Resonance Energy Transfer for Solid-Phase Bioassays and Biosensors. *Langmuir* **2017**, *33*, 12839–12858.

(10) Li, J.; Cushing, S. K.; Meng, F.; Senty, T. R.; Bristow, A. D.; Wu, N. Plasmon-induced resonance energy transfer for solar energy conversion. *Nature Photonics* **2015**, *9*, 601 – 607.

(11) Cushing, S. K.; Lie, J.; Meng, F.; Senty, T. R.; Suri, S.; Zhi, M.; Li, M.; Bristow, A. D.; Wu, N. Photocatalytic activity enhanced by plasmonic resonant energy transfer from metal to semiconductor. *J. Am. Chem. Soc.* **2012**, *134*, 15033–15041.

(12) Freyria, F. S.; Cordero, J. M.; Caram, J. R.; Doria, S.; Dodin, A.; Chen, Y.; Willard, A. P.; Bawendi, M. G. Near-Infrared quantum dot emission enhanced by stabilized self-assembled J-Aggregate Antennas. *Nano Lett.* **2017**, *17*, 7665–7674.

(13) Caram, J. R.; Doria, S.; Eisele, D. M.; Freyria, F. S.; Sinclair, T. S.; Rebentrost, P.; Lloyd, S.; Bawendi, M. G. Room-Temperature Micron-Scale Exciton Migration in a Stabilized Emissive Molecular Aggregate. *Nano Lett.* **2017**, *16*, 6808–6815.

(14) Rowland, C. E.; Fedin, I.; Zhang, H.; Gray, S. K.; Govorov, A. O.; Talapin, D. V.; Schaller, R. D. Picosecond energy transfer and multiexciton transfer outpaces Auger recombination in binary CdSe nanoplatlet solids. *Nat. Mater.* **2015**, *14*, 484–489.

(15) Pelzer, K. M.; Darling, S. B.; Gray, S. K.; Schaller, R. D. Exciton size and quantum transport in nanoplatelets. *J. Chem. Phys.* **2015**, *143*, 224106.

(16) Wang, C.; Weiss, E. A. Sub-Nanosecond Resonance Energy Transfer in the Near-Infrared within Self-Assembled Conjugates of PbS Quantum Dots and Cyanine Dye J-Aggregates. *J. Am. Chem. Soc.* **2016**, *138*, 9557 – 9564.

(17) Wang, C.; Weiss, E. A. Accelerating FRET between Near-Infrared Emitting Quantum Dots Using a Molecular J-Aggregate as an Exciton Bridge. *Nano Lett.* **2017**, *17*, 5666 – 5671.

(18) Thomas, R.; Thomas, A.; Pullanchery, S.; Joseph, L.; Somasundaran, S. M.; Swathi, R. S.; Gray, S. K.; Thomas, K. G. Plexcitons: The Role of Oscillator Strengths and Spectral Widths in Determining Strong Coupling. *ACS Nano* **2018**, *12*, 402 – 415.

(19) Choi, Y.; Kang, T.; Lee, L. P. Plasmon Resonance Energy Transfer (PRET)-based Molecular Imaging of Cytochrome c in Living Cells. *Nano Lett.* **2009**, *9*, 85–90.

(20) Karam, T. E.; Haber, L. H. Molecular Adsorption and Resonance Coupling at the Colloidal Gold Nanoparticle Interface. *J. Phys. Chem. C* **2014**, *118*, 642–649.

(21) Nascimento, D. R.; DePrince III, A. E. Modeling molecule-plasmon interactions using quantized radiation fields within time-dependent electronic structure theory. *J. Chem. Phys.* **2015**, *143*, 214104.

(22) Smith, H. T.; Karam, T. E.; Haber, L. H.; Lopata, K. Capturing Plasmon-Molecule Dynamics in Dye Monolayers on Metal Nanoparticles Using Classical Electrodynamics with Quantum Embedding. *The Journal of Physical Chemistry C* **2017**, *121*, 16932–16942.

(23) Wersäll, M.; Cuadra, J.; Antosiewicz, T. J.; Balci, S.; Shegai, T. Observation of Mode Splitting in Photoluminescence of Individual Plasmonic Nanoparticles Strongly Coupled to Molecular Excitons. *Nano Lett.* **2017**, *17*, 551–558.

(24) Brogersma, M. L.; Hartman, J. W.; Atwater, H. A. Electromagnetic energy transfer and switching in nanoparticle chain arrays below the diffraction limit. *Phys. Rev. B* **2000**, *62*.

(25) Maier, S. A.; Kik, P. G.; Atwater, H. A.; Meltzer, S.; Harel, E.; Koel, B. E.; Requicha, A. A. G. Local detection of electromagnetic energy transport below the diffraction limit in metal nanoparticle plasmon waveguides. *Nat. Mater.* **2003**, *2*, 229 – 232.

(26) Ilawe, N. V.; Oviedo, M. B.; Wong, B. M. Real-Time Quantum Dynamics of Long-Range Electronic Excitation Transfer in Plasmonic Nanoantennas. *J. Chem. Theory Comput.* **2017**, *13*, 3442–3454.

(27) Kuzyk, A.; Jungmann, R.; Acuna, G. P.; Liu, N. DNA Origamic Route for Nanophotonics. *ACS Photonics* **2018**, *5*, 1151 – 1163.

(28) Storhoff, J. J.; Mirkin, C. A. Programmed Materials Synthesis with DNA. *Chem. Rev.* **1999**, *99*, 1849 – 1862.

(29) Rosi, N. L.; Giljohann, D. A.; Thaxton, C. S.; Lytton-Jean, A. K. R.; Han, M. S.; Mirkin, C. A. Oligonucleotide-Modified Gold Nanoparticles for Intracellular Gene Regulation. *Science* **2006**, *312*, 1027 – 1030.

(30) Park, S. Y.; Lytton-Jean, A. K. R.; Lee, B.; Weigand, S.; Schatz, G. C.; Mirkin, C. A. DNA-Programmable Nanoparticle Crystallization. *Nature* **2008**, *451*, 553 – 556.

(31) Mirkin, C. A.; Letsinger, R. L.; Mucic, R. C.; Storhoff, J. J. A DNA-Based Method for Rationally Assembling Nanoparticles into Macroscopic Materials. *Nature* **1996**, *382*, 607 – 609.

(32) Cao, Y.; Jin, R.; Mirkin, C. DNA-Modified Core Shell Ag/Au Nanoparticles. *J. Am Chem. Soc.* **2001**, *123*, 7961 – 7962.

(33) Mitchell, G. P.; Mirkin, C. A.; Letsinger, R. L. Programmed Assembly of DNA Functionalized Quantum Dots. *J. Am. Chem. Soc.* **1999**, *121*, 8122 – 8123.

(34) Pathak, S.; Choi, S.; Arnheim, N.; Thompson, M. Hydroxylated quantum dots as luminescent probes for in situ hybridization. *J. Am. Chem. Soc.* **2001**, *123*, 4103 – 4104.

(35) Rosi, N. L.; Mirkin, C. A. Nanostructures in Biodiagnostics. *Chem. Rev.* **2005**, *105*, 1547 – 1562.

(36) Capek, I. *DNA Engineered Noble Metal Nanoparticles: Fundamentals and State-of-the-Art of Nanobiotechnology*; John Wiley and Sons, 2015.

(37) Zhang, N.; Han, C.; Xu, Y.-J.; Foley IV, J. J.; Zhang, D.; Codrington, J.; Gray, S. K.; Sun, Y. Near-field dielectric scattering promotes optical absorption by platinum nanoparticles. *Nat. Photon.* **2016**, *10*, 473–482.

(38) Zhang, J.; Jin, X.; Morales-Guzman, P. I.; Yu, X.; Liu, H.; Zhang, H.; Razzari, L.; Claverie, J. P. Engineering the Absorption and Field Enhancement Properties of AuTiO2 Nanohybrids via Whispering Gallery Mode Resonances for Photocatalytic Water Splitting. *ACS Nano* **2016**, *10*, 4496–4503.

(39) Codrington, J.; Eldabagh, N.; Fernando, K.; Foley IV, J. J. Unique Hot Carrier Distributions from Scattering-Mediated Absorption. *ACS Photon.* **2017**, *4*, 552–559.

(40) Rasamani, K. D.; Foley IV, J. J.; Beidelman, B.; Sun, Y. Enhanced optical absorption in semiconductor nanoparticles enabled by nearfield dielectric scattering. *Nano Res.* **2017**, *10*, 1292–1301.

(41) Rasamani, K. D.; Foley IV, J. J.; Sun, Y. One Stone Two Birds: Silica Nanospheres Enabling Significant Increase in Photocatalytic Activity and Colloidal Stability of Photocatalysts. *Nano Futures* **2018**, *1*, 015003.

(42) Chen, H.; McMahon, J. M.; Ratner, M. A.; Schatz, G. C. Classical Electrodynamics Coupled to Quantum Mechanics for Calculation of Molecular Optical Properties: a RT-TDDFT/FDTD Approach. *J. Phys. Chem. C* **2010**, *114*, 14384–14392.

(43) Skochdopole, N.; Mazziotti, D. A. Functional Subsystems and Quantum Redundancy in Photosynthetic Light Harvesting. *J. Phys. Chem. Lett.* **2011**, *2*, 2989–2993.

(44) Chin, A. W.; Datta, A.; Caruso, F.; Huelga, S. F.; Plenio, M. B. Noise-assisted energy transfer in quantum networks and light-harvesting complexes. *New J. Phys.* **2010**, *12*, 065002.

(45) Rebentrost, P.; Mohseni, M.; Kassal, I.; Lloyd, S.; Aspuru-Guzik, A. Environment-assisted quantum transport. *New J. Phys.* **2009**, *11*, 033003.

(46) Kholod, Y.; DeFilippo, M.; Reed, B.; Valdez, D.; Gillan, G.; Kosenkov, D. Excitation Energy Transfer Pathways in Light-Harvesting Proteins: Modeling with PyFREC. *J. Comp. Chem.* **2018**, *39*, 438–449.

(47) Hayes, D.; Engel, G. S. Peak shape analysis of diagonal and off-diagonal features in the two-dimensional electronic spectra of the Fenna-Matthews-Olson complex. *Phil. Trans. R. Soc. A* **2012**, *370*, 3692–3708.

(48) Hsu, L.-Y.; Ding, W.; Schatz, G. C. Plasmon-Coupled Resonance Energy Transfer. *The Journal of Physical Chemistry Letters* **2017**, *8*, 2357–2367.

(49) Krueger, B. P.; Scholes, G. D.; Fleming, G. R. Calculation of Couplings and Energy-Transfer Pathways between the Pigments of LH2 by the ab Inition Transition Density Cube Method. *J. Phys. Chem. B* **1998**, *102*, 5378–5386.

(50) Palik, E. D. *Handbook of optical constants of solids*; Academic Press, 1998.

(51) Johnson, P. B.; Christy, R. W. Optical constants of noble metals. *Phys. Rev. B* **1972**, *6*, 4370.

(52) Kraus, W. A.; Schatz, G. C. Plasmon resonance broadening in small metal particles. *J. Chem. Phys.* **1983**, *79*, 6130 – 6139.

(53) Coronado, E. A.; Schatz, G. C. Surface plasmon broadening for arbitrary shape nanoparticles: A geometrical probability approach. *J. Chem. Phys.* **2003**, *119*, 3926.

(54) Scholl, J. A.; Koh, A. L.; Dionne, J. A. Quantum plasmon resonances of individual metallic nanoparticles. *Nature* **2012**, *483*, 421–427.

(55) Peng, S.; McMahon, J. M.; Schatz, G. C.; Gray, S. K.; Sun, Y. Reversing the size-dependence of surface plasmon resonances. *Proc. Natl. Acad. Sci. U.S.A.* **2010**, *107*, 14530 – 14534.

(56) Sun, Y.; Foley IV, J. J.; Peng, S.; Li, Z.; K., G. S. Interfaced metal heterodimers in the quantum size regime. *Nano Lett.* **2013**, *13*, 3958–3964.

(57) He, Y.; Zheng, T. First-principles study and model of dielectric functions of silver nanoparticles. *J. Phys. Chem. C* **2010**, *114*, 18023–18030.

(58) Kumarasignhe, C.; Premaratne, M.; Agrawal, G. P. Dielectric function of spherical dome shells with quantum size effects. *Opt. Express* **2014**, *22*, 11966–11984.

(59) Mirkovic, T.; Ostroumov, E. E.; Anna, J. M.; van Grondelle, R.; Govindjee,; Scholes, G. D. Light Absorption and Energy Transfer in the Antenna Complexes of Photosynthetic Organisms. *Chem. Rev.* **2017**, *117*, 249–293.

(60) Indig, G. L.; Jay, D. G.; Grabowski, J. J. The efficiency of malachite green, free and protein bound, as a photon-to-heat converter. *Biophys. J.* **1992**, *61*, 631–638.

(61) Baranov, D. G.; Wersll, M.; Cuadra, J.; Antosiewicz, T. J.; Shegai, T. Novel Nanostructures and Materials for Strong LightMatter Interactions. *ACS Photonics* **2018**, *5*, 24–42.

Graphical TOC Entry